Material point simulations as a basis for determining Johnson-Cook hardening parameters via instrumented scratch tests

S. Leroch[a], S. J. Eder[a,b], M. Varga[a], M. Rodríguez Ripoll[a,*]

[a] *AC2T research GmbH, Viktor-Kaplan-Straße 2/C, 2700 Wiener Neustadt, Austria*
[b] *Institute of Engineering Design and Product Development, TU Wien, Lehárgasse 6 — Objekt 7, 1060 Vienna, Austria*

Abstract

Scratch tests are a powerful and inexpensive tool for studying the mechanical properties of materials. The tests are typically applied for determining the deformation behavior of materials and serves as quality assessment method for measuring the adhesion and delamination properties of coatings. However, the extraction of quantitative material parameters using scratch tests remains highly non-trivial and, contrary to instrumented indentation or tensile testing, a limited number of procedures are available so far for determining the hardening behavior of materials. Such procedures are of enormous relevance, since they allow a non-destructive determination of the material parameters of constitutive models commonly used in computer simulations for thin films, coatings, or surface changes due to loading. In this work we rely on extensive computational simulations of scratch tests using a meshless Material Point Method for finding relationships between the scratch forces, the scratch topography, and the material parameters. The simulations are performed for two large groups of metals with Young's moduli corresponding to steel and copper. Within each group, the yield stresses and hardening parameters are varied in order to cover the widest possible range of hardening behaviors. The results show that the scratch topography serves to narrow down the value of the yield stress, which can be alternatively determined using indentation. Once the yield stress is known, the hardening parameter can be unequivocally determined for a fixed hardening exponent via the scratch topography using a single scratch, or via the scratch forces using two scratches, provided that they are done at different normal loads.

Keywords: material point method; scratch test; Johnson-Cook model; wear; plasticity

1. Introduction

A scratch test is an experiment where a hard tip is displaced over a material surface under a controlled normal force in order to determine properties of the investigated surface [1]. This method, also named

*Corresponding author
Email address: ripoll@ac2t.at (M. Rodríguez Ripoll)

sclerometry, was initially proposed in 1722 [2] and subsequently popularized by Mohs a century later in 1822 using his well-known hardness scale based on 10 reference materials [3]. Since then, scratch tests have become a powerful and inexpensive tool, as they are particularly suitable for investigating the mechanical properties of those surfaces whose mechanical properties cannot be readily accessed using conventional mechanical tests, such as tensile, fracture, or fatigue tests [4]. This holds true in particular for small components or systems such as coatings and thin films, welding points, composite structures, or micro electro-mechanical systems [5]. In case of materials undergoing sliding or abrasive contact, the stresses imparted by a counterbody in the near-surface zone usually results in microstructural changes [6, 7, 8, 9, 10, 11, 12]. The heterogeneity of the resulting microstructure implies that while the mechanical properties of the near-surface zone dramatically differ from those of the bulk, their determination remains virtually impossible using conventional mechanical experiments [13, 14, 15, 16]. Scratch tests are nowadays mostly used to determine the properties of coatings and thin films. To this end, several standards have been proposed, such as the ISO 19252, ISO 20502, ASTM G171, ASTM D7027, or ASTM C1624, to name a few. The major limitation of these standards is that even though they provide quantitative data, such as scratch hardness, critical loads for crack initiation or delamination, their applicability for determining mechanical properties is limited. However, the determination of the yield stress and other mechanical parameters is crucial for determining the plastic behavior of materials. This applies in particular to computer simulations, which use constitutive models with material parameters that need to be known for each material, e.g., [17].

In contrast, some mechanical properties are accessible using instrumented indentation experiments. The pioneering work of Oliver and Pharr allowed the determination of hardness and reduced modulus using nanoindentation experiments [18]. Based on instrumented frictionless normal indentation, methodologies have been developed for estimating the yield strength and ductility of materials [18, 19, 20, 21]. However, while instrumented normal indentation is accurate for measuring the reduced Young's modulus, the prediction of yield strength is sensitive to small experimental errors [19, 20].

The determination of mechanical properties using scratch tests is not straightforward, as scratch testing involves a complex stress state that leads to various physical processes such as plastic deformation and material detachment. Despite the effort of many authors [22, 23, 5], a widely used and accepted method is still not available. Nevertheless, several authors made crucial contributions for determining the plastic properties of materials using instrumented scratch tests, which will be introduced in the following.

One of the first attempts applied dimensional analyses for defining scaling variables and universal functions [24]. Based on this, a methodology for determining the yield strength and strain hardening exponent of ductile materials was proposed using inverse analysis [5]. The method relies on dimensionless functions that are derived from computational simulations. The authors were then able to develop an algorithm for extracting the plastic properties of materials that follow an exponential plastic hardening law for the true flow stress.

The determination of the yield stress of materials using indentation tests has also been the subject of previous research. In some pioneering work, Tabor found that the yield strength of a material could be estimated by measuring the hardness and dividing its value by 3 [25]. This approximation, despite its shortcomings, has proved to be of high suitability for most engineering applications and has been widely used since then. In case of scratch tests, the relationship between scratch hardness and yield strength assuming an elastic-perfectly-plastic material was determined more recently using finite element analysis [26]. The

proposed model is thus suitable for determining the yield strength of materials when strain hardening is negligible. When considering strain hardening, other authors noted that the hardness during scratch testing of a elastic-perfectly-plastic material is between 2.5 and 3 times the yield strength [24].

The impact of the coefficient of friction during scratch testing on the elasto-plastic response of the material also needs to be considered when evaluating the link between scratch parameters and hardening response [27]. In this reference, the effect of Coulomb friction on the overall (apparent) coefficient of friction was investigated using finite element simulations as function of the hardening behavior. The authors developed a procedure for determining the Coulomb coefficient of friction. The most remarkable influence of friction on the scratch topography was an increase on the normalized burr height, and the results of the simulations were consistent with experimental scratch test results under dry and lubricated contact conditions. Interestingly, the authors observed in a later work that experimental errors associated with variations in hardness resulted in large errors in the estimation of the strain hardening exponent, while the material parameters were quite insensitive to variations in the adhesive coefficient of friction between indenter tip and material.

The previous works relying on the use of simulation tools as these, in contrast to scratch experiments, allow one to arbitrarily vary the hardening parameters of materials or keep them constant. The increase in computational power during the past decades made possible extensive computational simulations aimed at finding a link between the output of scratch tests and the hardening behavior of materials. Initially, most of the works relied on the use of the finite element method (FEM) [26, 24, 5, 27]. More recently, the use of meshless computational tools such as smooth particle hydrodynamics (SPH) or the material point method (MPM) for simulating scratch tests has gained increasing interest [28]. The advantages of meshless methods are that, in contrast to FEM, they can intrinsically deal with large deformations, material removal, and crack propagation, all of which are relevant in scratch tests [29, 30]. In a seminal work, we showed the feasibility of using SPH for simulating scratch tests, revealing good agreement with experimental data in terms of scratch forces and scratch topography [31]. Ever since, other authors have exploited the potential of such mesh-free methods as SPH [32, 33] and MPM [14, 34, 35, 36, 37, 38] for simulating scratch tests.

The aim of this work is to apply extensive computer simulations using an MPM model for finding relationships that can be exploited to determine plastic properties of materials. In contrast to most of the previous works that used an exponential plastic hardening law with two parameters, in our case we will focus on determining the material parameters of a Johnson-Cook based constitutive model [39]. The Johnson-Cook model is widely implemented in finite element codes and can be applied to describe the hardening behavior of a wide range of viscoplastic materials. The major novelty of our attempt is that we will aim to determine the material parameters using several scratches performed at different loads, in contrast to previous works that relied only on single scratches.

2. Models and simulation method

2.1. Material Point Method (MPM)

The MPM is a meshfree continuum method with explicit time integration, designed especially to study dynamic processes observed in cutting, scratching, or during impacts. MPM was developed by Sulsky [40] in the 1990s as a successor of the Particle-In-Cell (PIC) method. The aim was to apply the highly robust PIC methodology, originally designed for fluid flow problems, also to solid bodies. The equations of motion

(the particle velocity update) are integrated using a Particle in Cell (PIC), Fluid Implicit Particle (FLIP) approach with a mixing factor of 0.99 for FLIP to improve conservation of total energy and angular momentum while keeping the system numerically robust. MPM was further developed by many authors [41, 42] and successfully applied to a variety of solid body problems with large deformations and fracture. Common to all MPM schemes is the use of Lagrangian particles, i.e., the discretization of the material into deformable, non-overlapping particles, and the use of so-called kernel functions. To make the MPM numerically robust, an auxiliary regular background grid is also employed to compute strains and stresses. The current MPM model is described in more detail in Ref. [43]. In particular, our work uses the Generalized Interpolated Material Point (GIMP) Method [41]. This MPM version uses cubic B-splines for the shape functions as well as the Modified-updated-stress-last (MUSL) algorithm of Wallstedt [42] to improve the numerical stability and reduces the cell-crossing problem observed in conventional MPM and improves the convergence of the solution [44] (Algorithm 1 in the Supplementary Material). Even though GIMP with B-splines may not remove numerical fracture entirely, numerical fracture was not observed in the performed scratch simulations. The clear advantage of MPM over time explicit FEM methods lies in its nature, since the particles are discrete and interact only via their kernels, so it does not require additional separation formulations to allow fracture. MPM has been used before to simulate cutting and scratching of metals in good agreement with experiment [14, 43].

2.2. Constitutive Model

The material model is decomposed into isotropic and deviatoric parts, corresponding to volumetric and shear deformations. The relationship between the density ρ and the pressure p is given by the equation of state, while the relation between a tensorial shear deformation ϵ_d and the stress deviation tensor σ_d is given by the material strength model. The decomposition is additive, i.e.,

$$\sigma = -p\mathbf{I} + \sigma_{\mathbf{d}} \ , \tag{1}$$

where $\mathbf{I}$ is the diagonal unit tensor. The equation of state is assumed to be a linear relation between deformation gradient J and pressure,

$$p = -K(J-1) \ , \tag{2}$$

with K being the bulk modulus of the metal.

For the plastic yield stress we use the purely empirical Johnson-Cook (JC) plasticity model [39], which is numerically robust and therefore widespread in commercial finite element codes for thermal-elastic-plastic modeling:

$$\sigma_f(\epsilon, \dot{\epsilon}, T) = [A + B(\epsilon)^n][1 + C\ln(\dot{\epsilon^*})][1 - (T^*)^m] \ , \tag{3}$$

Here, ϵ is the equivalent plastic strain, which is calculated in dependence of the strain tensor, $\dot{\epsilon}$ its time derivative, the plastic strain rate, and A the material yield stress. B and n are strain hardening parameters, C a strain rate parameter, and m a temperature coefficient.

The normalized strain rate and temperature in Eq. (3) are defined as

$$\begin{aligned} \dot{\epsilon^*} &= \frac{\dot{\epsilon}}{\dot{\epsilon_0}} \\ T^* &= \frac{T - T_0}{T_m - T_0} \ , \end{aligned} \tag{4}$$

where $\dot{\epsilon_0}$ is the reference plastic strain rate, and T_0 the reference temperature at which the JC parameters have been parameterized, T_m is the reference melting temperature.

For the sake of simplicity, in the present work we neglect strain rate and temperature effects, as scratch tests are typically performed at low scratch velocities under quasistatic conditions. Hence, we used the following reduced formulation for the flow stress σ_f given as

$$\sigma_f(\varepsilon) = A + B\varepsilon^n \ . \tag{5}$$

To investigate the role of the JC parameters A, B, and n on the scratch forces and scratch topography, a parameter study was carried out. A, B and n were varied to obtain a high number of data in the parameter space, being fully aware that some of these combinations may not correspond to any existing material.

Moreover, to span a wide range of metals and alloys, two regions of Young's moduli were investigated. Starting from hard metals like steel and going to more ductile ones like copper. Thus, we selected the typical Young's moduli to be 210 and 120 GPa, respectively.

The selected values for the material properties of the two metal types can be found in Table 1, while the used set of JC parameters is shown in Table 2. Note that for the JC parameters, all possible combinations of A and B values were simulated.

Table 1: Material properties for steel taken from [43] and for copper from [31]: ρ is the reference bulk density, E Young's modulus, ν the Poisson ratio, C_p the specific heat capacity at room temperature, κ the heat conductivity.

	ρ (kg/m^3)	E (GPa)	ν	C_p (J/kg K)	κ (W/mK)
steel	7830	210	0.3	473	45
copper	8960	120	0.36	385	401

Table 2: Selected combinations of JC parameters A and B for steel and copper. The parameter n was set to 0.28 in all the cases.

steel		copper	
A (MPa)	B (MPa)	A (MPa)	B (MPa)
100	100	100	100
210	300	210	300
500	600	500	500
1050	1000	1050	800
2000	2000	2000	1500

In addition to the systems with constant n given in Table 2, selected systems with varying n were simulated for steel and copper as summarized in Table 3.

2.3. Computational setup

All the simulations were carried out with the open source code LAMMPS [45], applying the MPM user package available on request from the developer Ganzenmüller [43]. For the scratch simulations, metal blocks of sizes $1 \times 3 \times 0.4$ mm in x, y, z were created, with a particle resolution R of 10 μm and a cell width parameter for the auxiliary grid equal to R. Previous works have shown good agreement between

Table 3: Selected combinations JC parameters A and B for steel and copper with varying n. Note that all possible combinations of A and B values were simulated

steel			copper		
A (MPa)	B (MPa)	n	A (MPa)	B (MPa)	n
500	100	0.02	210	100	0.02
1050	300	0.2	500	300	0.2
	600	0.5		500	0.5

MPM simulations using the selected grid cell size or particle number per cell with finite element simulations and experiments [43]. The indenter is assumed completely rigid and of conical shape with a spherical tip of 200 μm radius (Rockwell C standard indenter) like in [14]. A scratch in y direction of 2 mm length was made at a scratch velocity of 100 m/s while constraining the lowest element layer of the metal. For an overview of the system and the scratch geometry nomenclature, see Fig. 1. A coefficient of friction of 0.4 was assumed (see Section 3.5), and the starting temperature of the substrate was set to room temperature. For every system the load was kept at constant and steady values of 20, 50, 70, and 100 N over 90% of the scratch distance, with negligible force variation for the material parameter combinations representing harder materials and no more than 10% error for the "soft" ones at high loads, see Fig. S1 for scratching distance resolved plots of the contact forces. The constant load was maintained using a proportional-integral algorithm to keep the surface of the substrate in a position so that the forces acting on it correspond to the specified value. By varying the JC parameters according to Table 2 for all metal types and loads, this results in a total of $5 \times 5 \times 4 \times 2 = 200$ scratch simulations. For the systems with varying n in Table 3, only loads of 20 and 70 N were applied, resulting in a total of $2 \times 3 \times 3 \times 2 \times 2 = 72$ additional simulations. The numerical load was manageable: on the VSC3 HPC computer, a single simulation on 64 cores took between 30 and 45 min depending on the Young's modulus.

2.4. Evaluation of the simulations

The post-processing of the simulation runs was carried out along the lines of the framework laid out in [32] for the dependence of forces on various parameters, while the topographic analysis for the evaluation of the geometrical shape of the scratches and derived quantities was performed similar to [14, 46].

The normal and transverse forces F_n and F_t, respectively, are output by LAMMPS in a time-resolved fashion and then filtered with a rectangular moving-average with a window width of 100 values (corresponding to 20 μm of scratching distance or 0.2 μs) for an assessment of their time-development. For the averaged values discussed later on in this work, the median force values between scratch distance 0.6 mm and 1.6 mm were calculated, thus omitting the indentation region as well as the end region that may be disproportionately characterized by build-up in front of the indenter. Error bars were obtained by calculating the standard deviation in the same scratching distance range. The slopes of the forces with respect to the scratch depth were obtained via a chi-square fit that was weighted according to the error bars of the respective data points.

The computational scratch topographies were first mapped to a mesh that was chosen slightly larger (22 μm) than the typical distance between the individual material points to prevent empty elements. The z-position of the highest material point within any element plus the material point radius then constituted

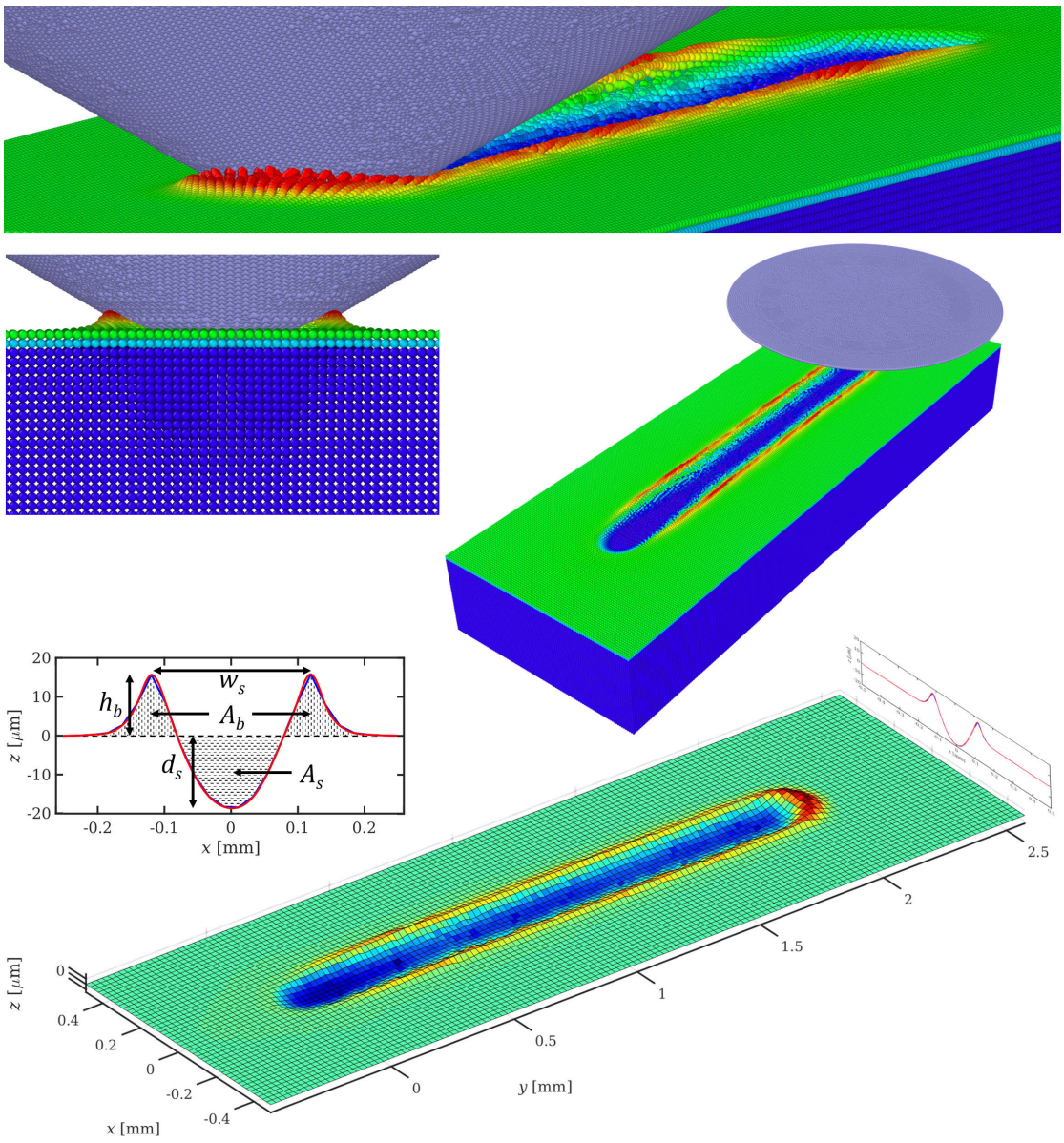

Figure 1: Overview of the simulation model at the example of Cu with $B = 500$ MPa and $A = 1050$ MPa at a load of 100 N. The lower part of the figure shows a meshed version of the scratched surface from which the median scratch profiles are calculated and an annotated graph of such a profile.

the topographic height of that element. As the geometry of the substrate is the same for all performed simulations, this geometry may be too narrow for soft materials at high loads, while it can lead to limitations in resolution for hard materials and lower force combinations. For these numerical reasons, as not all computed scratches are of the same length, median scratch profiles were calculated along the actual length of the scratches, thus again setting the focus on the central (steady-state) portions. The meshed scratch-profiles were then smoothed to a resolution of 1 μm using spline interpolants, which allows much more exact evaluation of all lateral and areal geometrical quantities. The scratch depth d_s represents the maximum depth below the original surface. The scratch width w_s was calculated as the distance between the two burr maxima, and the burr height h_b was calculated as the arithmetic mean of the two individual burr heights. Areal quantities such as the scratch A_s and burr A_b cross-sections, which serve as the basis for calculating the abrasive wear factor f_{ab}, were obtained via trapezoidal integration of the smoothed scratch profile portions between the appropriate surface intersection points.

Finally, based on the geometrical quantities calculated for an array of combinations of the yield stress A and the hardening coefficient B, we produced a set of 2D-maps of the key geometrical quantities as a function of A and B with a lateral resolution of 10 MPa (using a scattered interpolant), keeping the normal force, the material class, and the hardening exponent n constant.

2.5. Experimental scratch tests

Experimental scratch tests were performed on a high temperature scratch test developed at AC2T research GmbH, described in detail in [47]. As done in the MPM simulations, the scratches were performed with a rigid diamond indenter of Rockwell C geometry, i.e., a spherical tip of 200 μm radius on a 136° cone. The same loads as in the simulations were applied in the experiments, namely 20, 50, 70 and 100 N. The scratch velocity was set to 10 mm/min and the scratch length to 10 mm, in order to obtain stable scratch behavior. The array of scratches with increasing constant forces was repeated three times on the same sample for statistical assurance of the results. During the scratching procedure, online measurements of the normal force and tangential force were acquired to calculate the apparent coefficient of friction. As case study for steel, a commonly used R260 railway steel was investigated, featuring a fully pearlitic microstructure and 262±10 HV10 hardness or 2771±104 MPa. Furthermore, a high-strength CuNi alloy, Toughmet 160C, was used to compare results with the calculated maps for Cu–alloys. This material has an austenitic microstructure and 324±14 HV10 hardness or 3432±149 MPa.

After the experiments, the scratch topographies were measured using an Alicona® Infinite Focus G5 system. The topography data was pre-processed using Leica® Map software for repairing spurious missing data points, making an even surface level, and deskewing the orientations so that all scratches run horizontally and go from left to right.

After checking that all scratches are considerably longer than half the image width, longitudinal median values were calculated to simplify the 3D topographies to representative 2D scratch profiles that could be compared to the computational ones. Next, the scratch centers had to be identified by first masking the regions where the topography dropped below an appropriate z threshold and then searching for local minima within the masked regions. The mean values of the surface topography 0.8 mm away from the respective scratch center were reset to $z = 0$ to ensure that all height values (as well as the areal ones derived from them) were not marred by any offset. The corrected scratch cross-sections were then evaluated individually with respect to their key geometrical quantities, in principle analogous to the computational scratches.

However, as the lateral resolution was sufficient from the start (3.5 or 7.0 μm depending on the system), it was not necessary to smooth any experimental scratch profiles.

2.6. Tensile tests

Tensile tests were carried out in order to obtain stress-strain curves and fit the JC-parameters for verification of the scratch method. The tensile tests were done on a universal testing machine from Shimadzu with 100 kN maximum load. Standard round tensile samples with 8 mm sample diameter according to DIN 50125 were manufactured from the two materials. The tests were carried out at a quasistatic speed of 2 mm/min and repeated five times for statistical verification. The elongation of the samples was measured with a Sandner extensometer with 10 mm working distance for determining the true strain.

3. Results and discussion

3.1. Influence of the Johnson-Cook parameters on the scratch forces

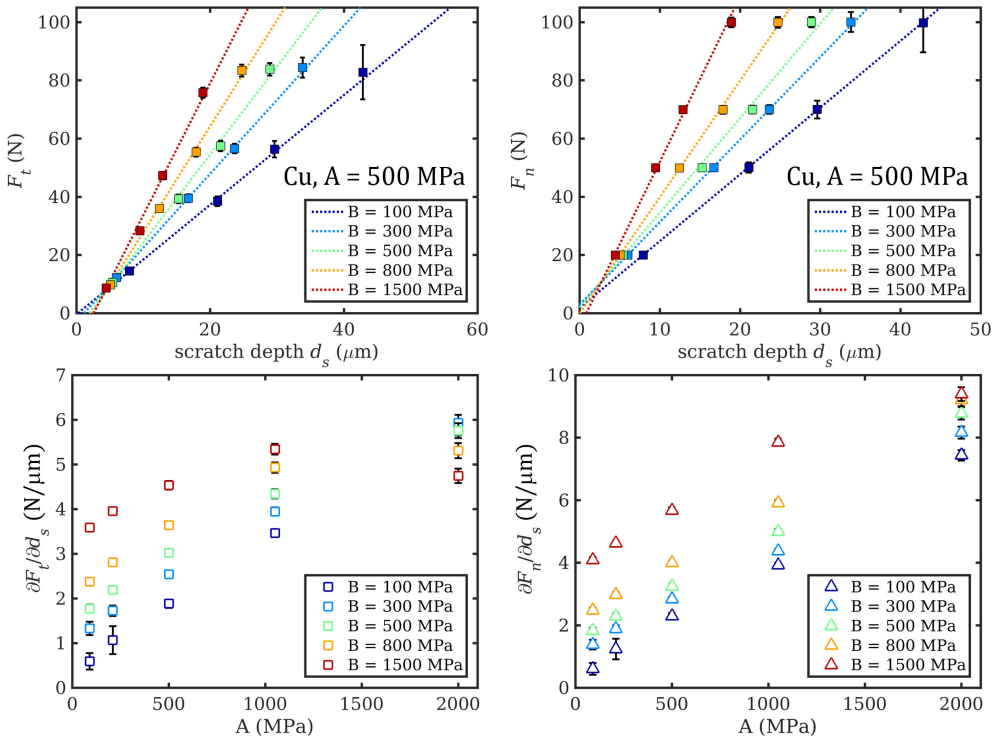

Figure 2: Top: representative graphs of the transverse (left) and normal forces (right) F_t and F_n, respectively, as a function of the scratch depth d_s for Cu with $A = 500$ MPa. Bottom: Overview of the corresponding slopes of the scratching forces with respect to d_s as a function of A. $n = 0.28$ in all graphs.

Figure 1 shows three snapshots of the MPM simulation from different perspectives. The elastoplastic material consists of particles displayed in different color, while the conical indenter is placed on top of the material block and shown in gray. The images show a representative overview of the conical indenter after sliding over the elastoplastic material. They illustrate the typical topography resulting from the scratching process. In general, the scratch topography is homogeneous throughout the length of the scratch. The burr height h_b also remains constant throughout most of the scratch length, and its height is only slightly lower or

higher at the initial and final sections of the scratch, respectively. The two bottom images show the meshed version of the elastoplastic material used for post-processing and extracting the median scratch profiles that serve as a basis for systematically evaluating all simulations.

For a given material, defined by a combination of yield stress A, hardening parameter B, and hardening exponent n, the applied normal load F_n and the resulting tangential force F_t during the scratch simulation are plotted as function of the scratch depth in Fig. 2. For a given combination of material parameters A and B, an increase in the applied normal load F_n results in a linear increase of the scratch depth d_s. The same linear behavior is observed between the tangential scratch force F_t and depth. The results also highlight that for a fixed yield stress A, an increase in the hardening parameter B results in a higher slope.

Based on this linear relation between F_n and F_t with d_s, the slopes of the applied normal load and the scratch force against the scratch depth are plotted versus the yield stress A for the different hardening parameters B, see Fig. 2. The results show that the slope $\partial F_t/\partial d_s$ increases rapidly for smaller yield stresses, while for higher A values, the slope seems to saturate or even slightly decrease for large B values. It should be noted that for extreme values of the yield stress, the deformation imparted by the indenter was extremely small and consequently less accurate when compared to simulations using softer materials. In case of the slope $\partial F_n/\partial d_s$, the trend as function of A seems to follow a similar dependence, with the main difference that the slope keeps rising even for large A values. Figure 2 illustrates that for materials with known yield stress A, it is possible to determine the value of B by only performing two experimental scratch tests at different applied normal loads, if we assume a hardening exponent value of n=0.28. Analogous plots could be also obtained for arbitrary hardening exponent values n.

3.2. Influence of the Johnson-Cook parameters on the scratch topography

Besides the scratch forces, additional valuable information of the hardening behavior of materials can be obtained by analyzing the scratch topography. The dependence of the burr cross-section, scratch cross-section, and abrasive wear factor f_{ab} on the yield stress A for all simulated B values is shown in Figure 3 for copper and steel. The results reveal that the values of the burr and the scratch cross-sections allow us to narrow down the value of the yield stress A, as larger values of the burr and scratch cross-section are only possible for small values of A, independently of the value of B. Considering the f_{ab} parameter, its values as function of A follow an unclear trend that complicates the extraction of useful information regarding B. This may be partially attributed to the way f_{ab} is defined as the ratio of quantities that are not independent of each other, so that slight variations in the assumption of the $z = 0$ line/plane can have a large influence on the value of f_{ab}. As mentioned in the previous section, the data obtained is valid for a hardening exponent value of $n = 0.28$.

The topography parameters A_b, A_s and f_{ab} are selected for evaluation, as they do not trivially depend on one another. In case of scratch depth and scratch width, both parameters are not independent of the scratch cross-section, since all of them are determined by the geometry of the indenter, as illustrated in Fig. 4. Regarding the burr cross-section and the burr height, their values correlate with those of the scratch depth for high B values, while for lower values of B they deviate.

3.3. Hardening parameter maps

All simulated values of the burr cross-section A_b, burr height h_b, scratch cross-section A_s, scratch depth d_s, and abrasive wear factor $f_{ab} = (A_s - A_b)/A_s$ can be plotted as functions of A and B using heat maps, as

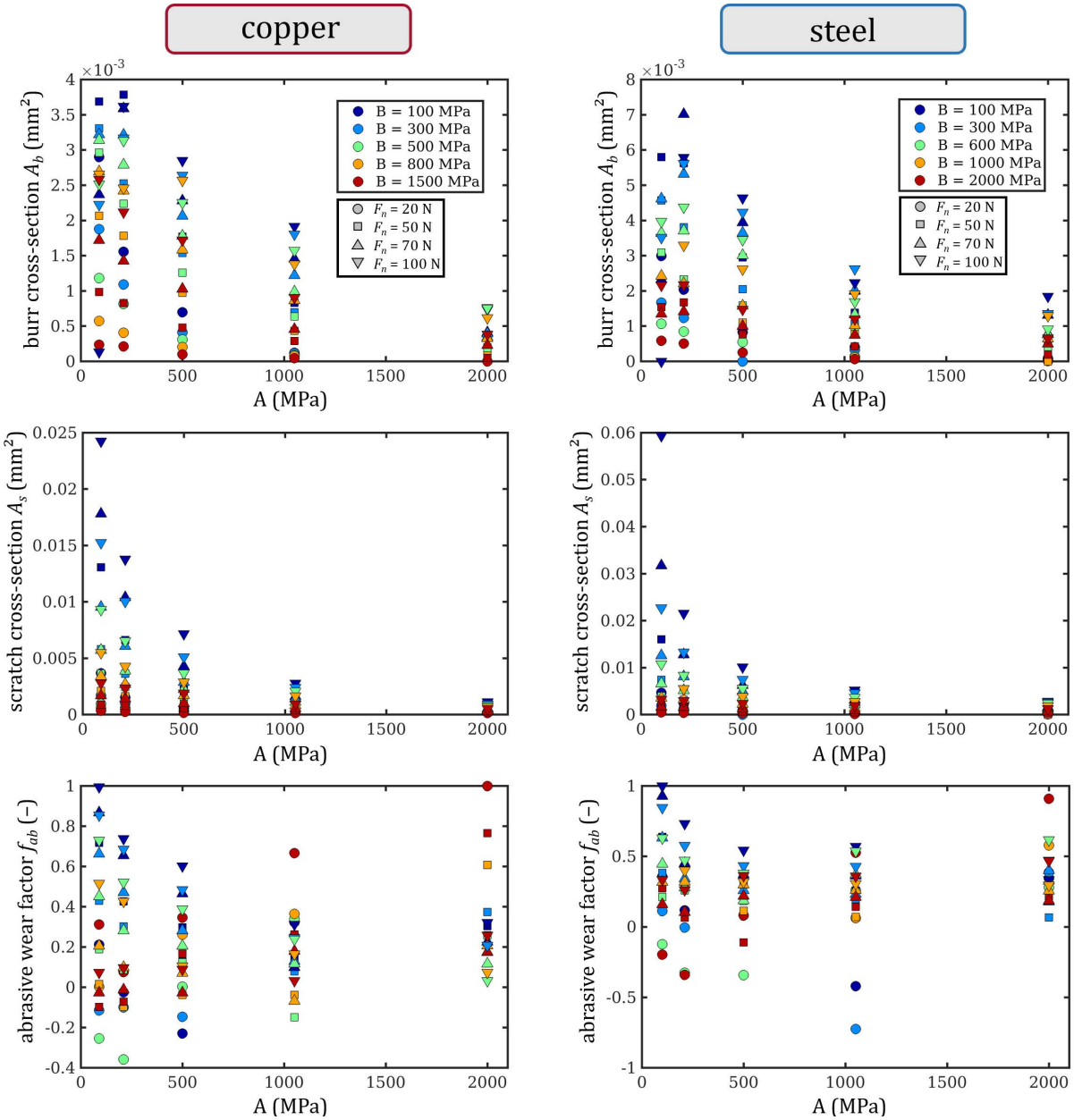

Figure 3: Cross-section areas of burr A_b and scratch A_s, as well as the abrasive wear factor f_{ab} as a function of A for various values of B. B is color-coded, and different normal forces F_n are represented as different symbols. $n = 0.28$ in all graphs.

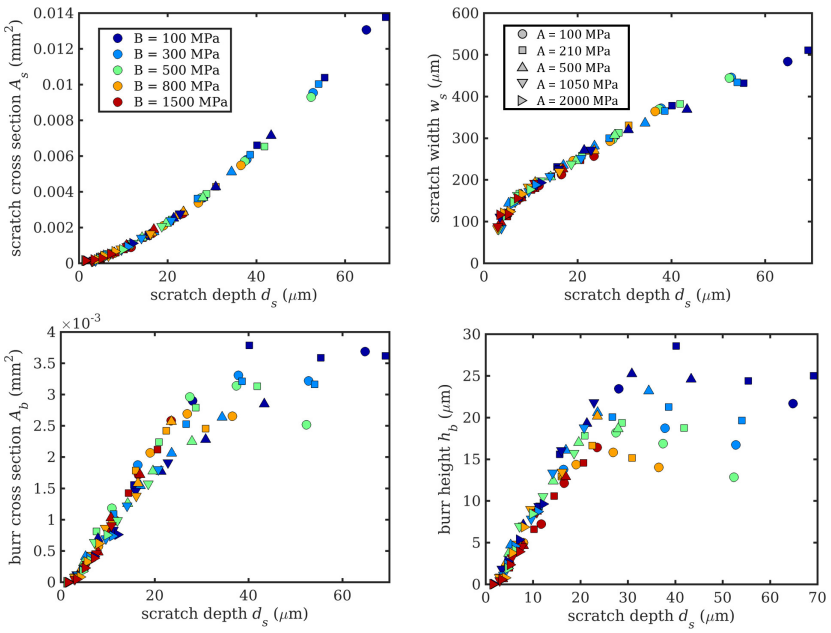

Figure 4: Some general global correlations between geometrical quantities and the scratch depth (here representative data for Cu).

shown in Fig. 5. The values of scratch cross-section and scratch depth diminish for combinations involving higher values of A and B. In case of the burr height, the trend is similar for larger values of B. For smaller values, the relation between A and B becomes more complex. Finally, the relation of A and B with the factor f_{ab} is more complex, and an "island" of lower f_{ab} values can be observed for intermediate values of A and B. The abrasive wear factor is intended for values ranging from 0 (pure plowing) to 1 (pure cutting). In our case, isolated simulations lead to f_{ab} values below zero. This occurs mostly when the scratches are so shallow that they are poorly resolved with the chosen MPM element size. In addition, near-surface matter from the initial indentation location may have been pushed into the ridges of the evaluation range, compounding this effect, as the range over which we average along the scratch direction to produce the median scratch cross-sections does not cover the entire scratching length of 2 mm, but rather only the 1 mm near the center that is least affected by pure indentation and the pile-up in front of the indenter pushed to the end of the scratch. It is therefore possible that certain parameter combinations produce median scratch cross-sections where the ridge-area is seemingly larger than the scratch-area.

The heat maps reveal that for a given topographic quantity, the knowledge of its value allows one to find possible combinations of A and B for describing this material. A unique determination of A and B is not possible by knowing only one of these parameters.

3.4. Influence of the hardening exponent n on the scratch forces and scratch topography

In the previous sections, the influence of the Johnson-Cook hardening parameters A and B on the derivative of the scratch forces versus the scratch depth and the scratch topography has been taken into account, while keeping n constant at a value of $n = 0.28$. In what follows, the influence of n on the scratch forces is investigated for several combinations of A and B, see Table 3. The results of the simulations are shown in the Supplementary Material. Figure S2 shows that for copper alloys, a variation of n between

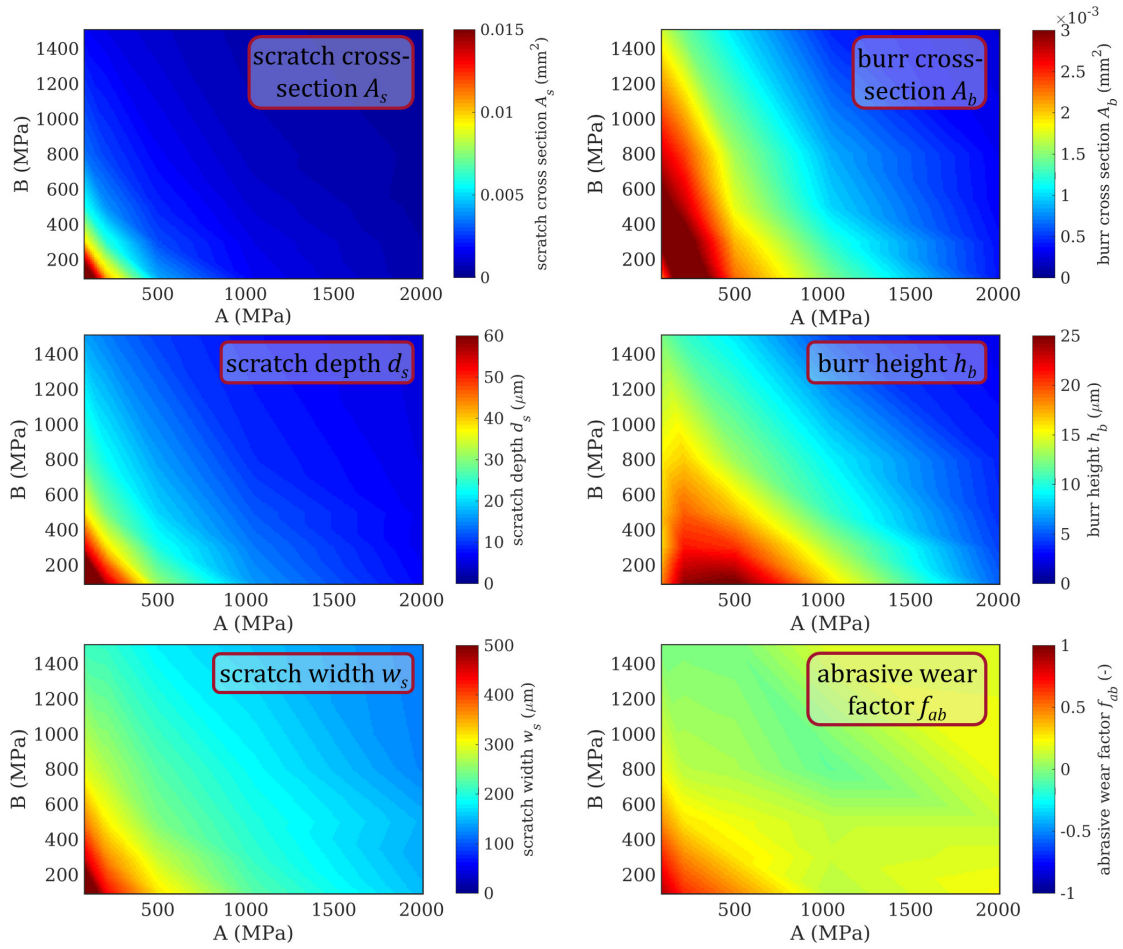

Figure 5: Representative heat maps of geometrical quantities from simulations for Cu at a load of 70 N as a function of A and B.

0.02 and 0.5 results in little changes in the derivative of the tangential scratch force F_t by the scratch depth d_s, as the differences in tangential force values differ less than 10 % (not shown). The only exception is observed for $n = 0.02$ for $A = 210$ MPa and $B = 500$ MPa, which is an outlier due to numerical instabilities. In case of steel, the variation is small for low values of the hardening modulus B, but the influence of n increases with its value, being more pronounce for $B = 600$ MPa. This is clearly illustrated in the plot of the derivative of the tangential scratch force by the scratch depth ($\partial F_t/\partial d_s$) versus the value of exponent n, see the bottom row of Fig. S2. In case of copper, for a given A and B value, the points lie within an almost horizontal line (with the exception of the outlier) for values of n ranging from 0.02 and 0.5. In contrast, the results obtained for steel show that for $B = 100$ MPa, the derivative value remains constant for all n values. For $A = 500$ MPa, the derivative follows a linear increase for increasing n values, when B lies between 300 and 600 MPa. In case of steels with a higher yield of $A = 1050$ MPa, the derivative remains constant for values of n smaller than 0.2, while its value decreases for $n = 0.5$.

The impact of n on the scratch geometry is shown in Fig. S3. The results show a weaker dependence on n for the burr and the scratch cross-section at smaller normal loads (lower group of symbols in the plots). At higher loads, the influence of n increases, being higher for lower yield stress values (cf. the upper groups of symbols).

3.5. Influence of the coefficient of friction on the scratch forces and scratch topography

Throughout the present work, the value of the Coulomb coefficient of friction was set to 0.4. The value of the coefficient of friction during scratch testing has been experimentally investigated by several authors. For instance, Bowden and Young reported in 1951 that Rowe (unpublished) measured a coefficient of friction of 0.4 in air between copper and a small curved diamond indenter for an applied load of 0.25 N [48]. In more recent work, the coefficient of friction during scratch testing between a diamond Rockwell indenter and copper was experimentally estimated to be 0.1. In this case the authors performed several scratches at different loads and observed that the apparent coefficient of friction increased with applied scratch load and saturated at a value of 0.8. By decomposing the apparent coefficient of friction into two additive components, a deformation component and a Coulomb component, a constant value of 0.1 fairly independent of the load could be assessed.

In order to evaluate the impact of the coefficient of friction on the scratch forces and scratch geometry, a selected number of scratch simulations was performed with a coefficient of friction value of 0. The simulations account for two values of the yield stress A, namely 210 and 1050 MPa, and two values for the hardening parameter B (300, 800 GPa), and were performed at two different applied normal loads (20 and 70 N). A comparison of the results shown in Fig. S4 with those from Fig. 3 illustrates that for copper, the scratch cross-section A_s is robust against drastic changes in friction, with small differences even for high yield stress values of $A = 1050$ MPa. In contrast, the burr cross-section A_b is more sensitive to friction, therefore one should preferably rely on the A_s for determining the material parameters whenever possible. In case of steel, the values feature more scattering when compared to copper. Also in this case, the values obtained for a yield stress A of 210 MPa are less sensitive to changes in Coulomb coefficient of friction when compared to values exceeding 1 GPa.

3.6. Case study using a copper and a steel alloy

In what follows, we use a case study for illustrating the applicability of the simulation results obtained in this work for determining the Johnson-Cook parameters A and B of copper alloys and steel. The case study

uses a high-performance Toughmet 160C CuNi alloy and a widely used railway steel grade R260. The former has a high yield stress, but a very low hardening rate, resulting in hardening behavior close to an ideally plastic material. On contrary, the railway steel, with its fully pearlitic microstructure, is characterized by a large hardening rate (Fig. S5 in the Supplementary Material). The experimental scratches were performed on both alloys at 20, 50, 70 and 100 N. The surface topography measurements of the scratches are shown in Fig. 6 along with their averaged cross-section profiles. as it can be observed, the scratch depth and burr height increased for higher applied scratch normal loads. In case of scratches performed at 20 N, the degree of plastic deformation was too small and for this reason, these values were not used in what follows. Besides the scratch topography, the applied normal and tangential forces are continuously monitored throughout the experiment. Additional Vickers indentations were performed on both alloys in order to provide an estimate of the yield stress according to Tabor.

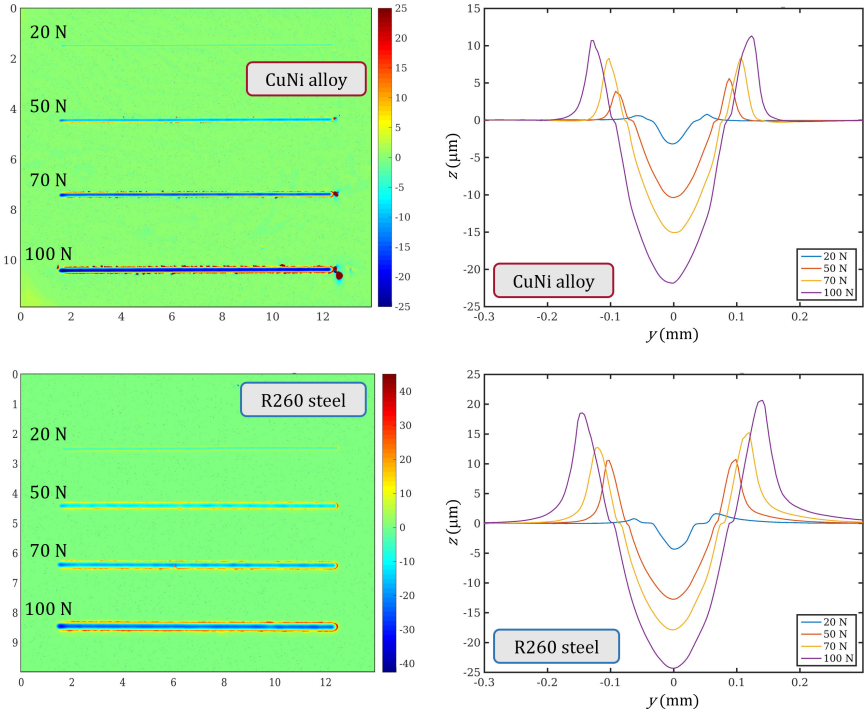

Figure 6: Experimental scratch topographies and median scratch profiles for a high-performance CuNi alloy and an R260 steel.

The topography data of the experimental scratches can be used to read the value of the hardening parameters using the parameter maps developed in Section 3.3. The results are shown in Fig. 7. For the three experimental scratch loads of 50, 70, and 100 N, a contour line is drawn in the corresponding simulated parameter map (cf. Fig. 5) for every measured value of the scratch width, scratch depth, and burr height. The contour lines show that for both alloys, there exists a combination of A and B values that are consistent with the measured topography. In case of the CuNi alloy, the values determined for A and B are almost identical, independently of the normal load applied for the scratch. This holds particularly well for the scratch width and the scratch depth. In case of the burr height, the agreement is excellent for the smallest scratch loads, while at the largest loads, the topography data predicts a harder material. In case of the R260 steel, there is a higher deviation for the A and B values determined from the parameter maps, but

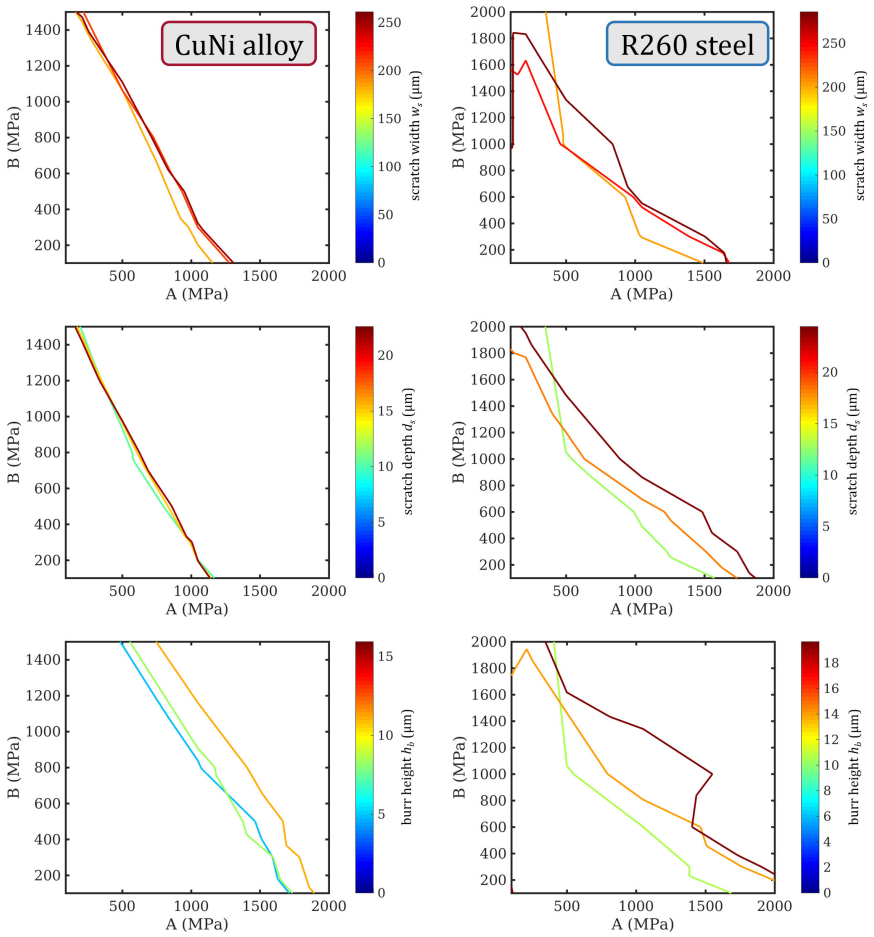

Figure 7: Contours of experimentally measured geometrical scratch properties (color-coded for the three highest scratch loads; 20 N was omitted due to insufficient scratch depth) of the high-performance CuNi alloy and the R260 steel, plugged into the computationally obtained maps for Cu and Fe alloys (as shown for Cu in Fig. 5). Every iso-curve corresponds to one experimentally obtained geometrical quantity.

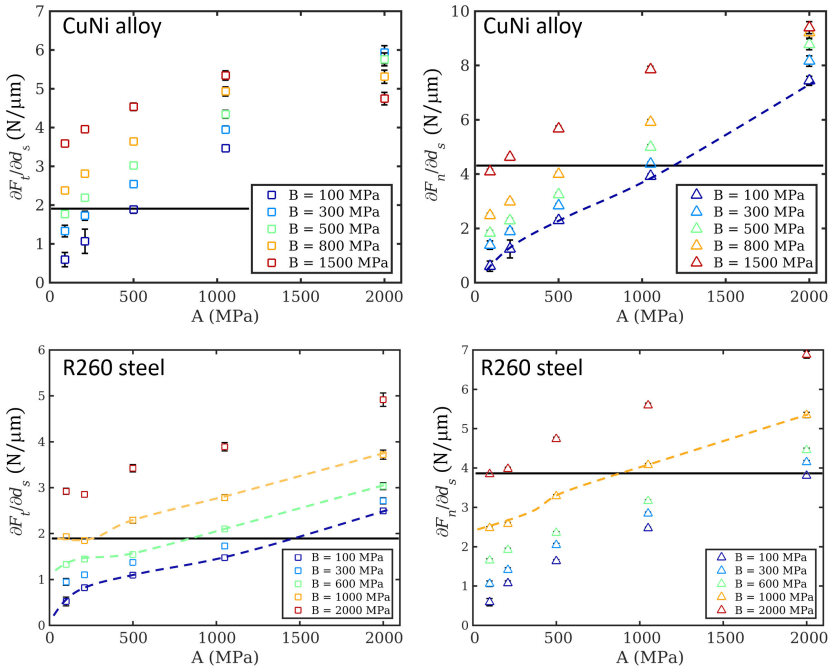

Figure 8: Force slopes vs. experimental results. Intersections between solid black lines (experimental results) and dashed colored lines are consistent with Fig. 7.

the values predicted using different topography parameters such as the scratch width, the scratch depth, and the burr height are in good agreement. Based on the topography data alone, it is possible to apply the parameter maps to restrict the possible combinations of A and B values, but a unique determination is not possible. The value of A can be narrowed down based on the measurements. For example, the maximum scratch depth d_s measured for steel (values for CuNi in parentheses) was 24.4 μm (21.9 μm) for 100 N, a burr cross-section A_b of 2115 μm^2 (830 μm^2), and a scratch cross-section A_s of 3116 μm^2 (2585 μm^2). Based on the results shown in Figure 3, this allows us to restrict A to values below 1500 MPa (1200 MPa). A further relation between the A and B hardening parameters is available via the slopes of the scratch forces as function of the scratch depth. By using this relation, as shown in Figure 2, it is possible to see that the horizontal given by the value of the slope cuts possible combinations of A and B values, even though, as in case of the topography, a unique determination of both values is not possible *a priori*. An alternative is to determine the value of A by indentation following Tabor [25], or applying a similar approach using scratch tests [26, 24]. In our case, the use of Tabor leads to an estimate value of $A = 1144$ MPa for the CuNi alloy and 924 MPa for R260 steel. Once the parameter A is fixed, the value of B can be trivially determined with a single scratch test using either the parameter maps or with two scratch tests via the slope of the scratch force vs. scratch depth. Using the former, the estimated value for CuNi is $B = 150$ MPa, while using the latter it is $B = 100$ MPa. In case of steel R260, the determined values of B would be 900 and 1000 MPa, respectively. As seen in this example, the results given by the forces compare well with the values obtained using the scratch topography, highlighting the consistency of our approach.

In order to verify the accuracy of the hardening parameters obtained using scratch tests, uniaxial tensile tests were performed for obtaining stress-strain curves, see Fig. S5 in the Supplementary Material. Five

independent measurements were done on each alloy. Afterwards, these data were used to fit the Johnson-Cook model and determine the best fit for the hardening parameters. For the fitting procedure, two different approaches were pursued. In the first one, all three hardening parameters A, B, and n were simultaneously determined (black curves in Fig. S5). In a second approach, only the values of A and B were fitted, while the value of n was fixed to 0.28, as done in most of the MPM simulations (red curves in Fig. S5). The values obtained from the fitting are given in Table 4.

Table 4: Johnson Cook parameters fit from experiment

material	A (MPa)	B (MPa)	n
R260 steel	550	2200	0.45
	695	1000	0.28
CuNi	1130	82	0.22
	1130	100	0.28

The best fit for the CuNi alloy is done with a n value close to the 0.28 value used in the simulations. In case of the R260 steel, the best value for n is 0.4, with $B = 1850$ MPa. However, the stress-strain data can also be reproduced satisfactorily assuming an n of 0.28 with $B = 1200$ MPa. If we compare these fitting values with the values obtained using the scratch simulations, we can see that the accuracy of the estimation of B is very good once A is determined. The accuracy seems to be better for materials with a low hardening rate, where the assumption of a smaller hardening exponent n also holds. For materials with a high hardening rate, the determination of A via Tabor is less accurate, as Tabor determines the yield strength, which can be substantially larger than the yield stress for materials with a high hardening rate. Also in this case, the assumption of an n exponent with a value of 0.28 provides a less accurate fit for the uniaxial experiments.

4. Conclusion

The present work has investigated the feasibility of determining the hardening behavior of metals using scratch tests. The slope of the normal and tangential force versus the scratch depth allows one to determine either the yield stress or the hardening modulus using two scratch tests at different normal loads, provided that one of the quantities is known before hand. Based on a geometrical analysis of the scratches, we can narrow down the allowed values of the yield stress. From the obtained simulated data, it was possible to generate parameter maps for determining the yield stress or the hardening modulus as a function of geometric scratch characteristics. However, these maps still require prior knowledge of one of the hardening parameters, such as the yield stress. A case study using a high performance copper alloy and a pearlitic railway steel shows that after determining the yield stress using indentation hardness, a good estimate of the hardening modulus can be obtained without the need for tensile tests. The presented scratch topography maps are a powerful tool that can be readily used to estimate the material parameters of the Johnson-Cook model, a plasticity model widely implemented in finite element codes. Additionally, the presented maps can be subsequently extended to include other engineering-relevant alloys and take into account strain rate dependence and temperature. The ultimate goal is the complete determination of hardening parameters by exclusive use of scratch tests as an alternative to conventional uniaxial experiments.

5. Acknowledgment

This work was funded by the Austrian COMET-Program (Project K2 InTribology1, no. 872176) and carried out at the Austrian Excellence Center for Tribology (AC2T research GmbH). The presented computational results were obtained in part using the Vienna Scientific Cluster (VSC).

References

[1] V Jardret, H Zahouani, Jean-Luc Loubet, and TG Mathia. Understanding and quantification of elastic and plastic deformation during a scratch test. *Wear*, 218(1):8–14, 1998.

[2] A Djamai, H Zaidi, KJ Chin, and T Mathia. Damage identification of dlc coating by microscratch test. In *Tribology and Interface Engineering Series*, volume 51, pages 223–231. Elsevier, 2006.

[3] Friederich Mohs. Grund-Riß der Mineralogie, Erster Theil: Terminologie, Systematik, Nomenklatur, Charakteristik. *Dresden, Arnoldische Buchhandlung*, 1822.

[4] Kenneth Holmberg, Anssi Laukkanen, Helena Ronkainen, Kim Wallin, and Simo Varjus. A model for stresses, crack generation and fracture toughness calculation in scratched tin-coated steel surfaces. *Wear*, 254(3):278–291, 2003.

[5] SC Bellemare, M Dao, and S Suresh. A new method for evaluating the plastic properties of materials through instrumented frictional sliding tests. *Acta materialia*, 58(19):6385–6392, 2010.

[6] Christian Greiner, Johanna Gagel, and Peter Gumbsch. Solids under extreme shear: Friction-mediated subsurface structural transformations. *Advanced Materials*, 31(26):1806705, 2019.

[7] Ao Li and Izabela Szlufarska. How grain size controls friction and wear in nanocrystalline metals. *Physical Review B*, 92(7):075418, 2015.

[8] H Rojacz, G Mozdzen, F Weigel, and M Varga. Microstructural changes and strain hardening effects in abrasive contacts at different relative velocities and temperatures. *Materials Characterization*, 118:370–381, 2016.

[9] H Rojacz, M Premauer, and M Varga. Alloying and strain hardening effects in abrasive contacts on iron based alloys. *Wear*, 410:173–180, 2018.

[10] Stefan J Eder, Philipp G Grützmacher, Manel Rodríguez Ripoll, Daniele Dini, and Carsten Gachot. Effect of temperature on the deformation behavior of copper nickel alloys under sliding. *Materials*, 14(1):60, 2021.

[11] SJ Eder, PG Grützmacher, M Rodríguez Ripoll, and JF Belak. Elucidating the onset of plasticity in sliding contacts using differential computational orientation tomography. *Tribology Letters*, 69(3):1–15, 2021.

[12] SJ Eder, PG Grützmacher, Thomas Spenger, H Heckes, H Rojacz, A Nevosad, and Franz Haas. Experimentally validated atomistic simulation of the effect of relevant grinding parameters on work piece topography, internal stresses, and microstructure. *Friction*, pages 1–22, 2021.

[13] J. Michler, R. Rabe, J.-L. Bucaille, B. Moser, P. Schwaller, and J.-M. Breguet. Investigation of wear mechanisms through in situ observation during microscratching inside the scanning electron microscope. *Wear*, 259(1):18–26, 2005. 15th International Conference on Wear of Materials.

[14] M Varga, S Leroch, SJ Eder, H Rojacz, and M Rodríguez Ripoll. Influence of velocity on high-temperature fundamental abrasive contact: A numerical and experimental approach. *Wear*, 426:370–377, 2019.

[15] M Varga, S Leroch, T Gross, H Rojacz, SJ Eder, M Grillenberger, and M Rodríguez Ripoll. Scratching aluminium alloys–modelling and experimental assessment of damage as function of the strain rate. *Wear*, 476:203670, 2021.

[16] SJ Eder, S Leroch, PG Grützmacher, T Spenger, and H Heckes. A multiscale simulation approach to grinding ferrous surfaces for process optimization. *International Journal of Mechanical Sciences*, 194:106186, 2021.

[17] A Rudnytskyj, M Varga, S Krenn, G Vorlaufer, J Leimhofer, M Jecha, and C Gachot. On the relationship of surface hardness and bulk flow stress in metal forming. *Mechanics of Materials*, page submitted, 2022.

[18] Warren Carl Oliver and George Mathews Pharr. An improved technique for determining hardness and elastic modulus using load and displacement sensing indentation experiments. *Journal of materials research*, 7(6):1564–1583, 1992.

[19] M Dao, N v Chollacoop, KJ Van Vliet, TA Venkatesh, and SJAM Suresh. Computational modeling of the forward and reverse problems in instrumented sharp indentation. *Acta materialia*, 49(19):3899–3918, 2001.

[20] Andrew Gouldstone, Nuwong Chollacoop, Ming Dao, Ju Li, Andrew M Minor, and Yu-Lin Shen. Indentation across size scales and disciplines: Recent developments in experimentation and modeling. *Acta Materialia*, 55(12):4015–4039, 2007.

[21] Yang-Tse Cheng and Che-Min Cheng. Scaling, dimensional analysis, and indentation measurements. *Materials Science and Engineering: R: Reports*, 44(4-5):91–149, 2004.

[22] J.L Bucaille, E Felder, and G Hochstetter. Mechanical analysis of the scratch test on elastic and perfectly plastic materials with the three-dimensional finite element modeling. *Wear*, 249(5):422–432, 2001.

[23] Eric Felder and Jean-Luc Bucaille. Mechanical analysis of the scratching of metals and polymers with conical indenters at moderate and large strains. *Tribology International*, 39(2):70–87, 2006. 180 Years of Scratch Testing.

[24] S Bellemare, M Dao, and S Suresh. The frictional sliding response of elasto-plastic materials in contact with a conical indenter. *International Journal of Solids and Structures*, 44(6):1970–1989, 2007.

[25] David Tabor. A simple theory of static and dynamic hardness. *Proceedings of the Royal Society of London. Series A. Mathematical and Physical Sciences*, 192(1029):247–274, 1948.

[26] Ki Myung Lee, Chang-Dong Yeo, and Andreas A Polycarpou. Relationship between scratch hardness and yield strength of elastic perfectly plastic materials using finite element analysis. *Journal of Materials Research*, 23(8):2229–2237, 2008.

[27] SC Bellemare, M Dao, and S Suresh. Effects of mechanical properties and surface friction on elasto-plastic sliding contact. *Mechanics of Materials*, 40(4-5):206–219, 2008.
[28] Alban de Vaucorbeil, Vinh Phu Nguyen, Sina Sinaie, and Jian Ying Wu. Material point method after 25 years: Theory, implementation, and applications. In *Advances in applied mechanics*, volume 53, pages 185–398. Elsevier, 2020.
[29] Alban de Vaucorbeil and Christopher R Hutchinson. A new total-lagrangian smooth particle hydrodynamics approximation for the simulation of damage and fracture of ductile materials. *International Journal for Numerical Methods in Engineering*, 121(10):2227–2245, 2020.
[30] Alban de Vaucorbeil and Vinh Phu Nguyen. Modelling contacts with a total lagrangian material point method. *Computer Methods in Applied Mechanics and Engineering*, 373:113503, 2021.
[31] S Leroch, M Varga, S J Eder, A Vernes, M Rodriguez Ripoll, and G Ganzenmüller. Smooth particle hydrodynamics simulation of damage induced by a spherical indenter scratching a viscoplastic material. *International Journal of Solids and Structures*, 81:188–202, 2016.
[32] M Varga, S Leroch, SJ Eder, and M Rodríguez Ripoll. Meshless microscale simulation of wear mechanisms in scratch testing. *Wear*, 376:1122–1129, 2017.
[33] M Varga, S Leroch, H Rojacz, and M Rodríguez Ripoll. Study of wear mechanisms at high temperature scratch testing. *Wear*, 388–389:112–118, 2017.
[34] Tanmaya Mishra, Matthijn de Rooij, Meghshyam Shisode, Javad Hazrati, and Dirk J Schipper. Characterization of interfacial shear strength and its effect on ploughing behaviour in single-asperity sliding. *Wear*, 436:203042, 2019.
[35] Tanmaya Mishra, Georg C Ganzenmüller, Matthijn de Rooij, Meghshyam Shisode, Javad Hazrati, and Dirk J Schipper. Modelling of ploughing in a single-asperity sliding contact using material point method. *Wear*, 418:180–190, 2019.
[36] MA Mekicha, MB de Rooij, T Mishra, DTA Matthews, L Jacobs, and DJ Schipper. Study of wear particles formation at single asperity contact: An experimental and numerical approach. *Wear*, 470:203644, 2021.
[37] Tanmaya Mishra, Matthijn de Rooij, and Dirk J Schipper. The effect of asperity geometry on the wear behaviour in sliding of an elliptical asperity. *Wear*, 470:203615, 2021.
[38] Alban de Vaucorbeil, Vinh Phu Nguyen, Christopher R Hutchinson, and Matthew R Barnett. Total lagrangian material point method simulation of the scratching of high purity coppers. *International Journal of Solids and Structures*, page 111432, 2022.
[39] Gordon R Johnson and William H Cook. Fracture characteristics of three metals subjected to various strains, strain rates, temperatures and pressures. *Engineering fracture mechanics*, 21(1):31–48, 1985.
[40] Deborah Sulsky, Zhen Chen, and Howard L Schreyer. A particle method for history-dependent materials. *Computer methods in applied mechanics and engineering*, 118(1-2):179–196, 1994.
[41] S. G. Bardenhagen and E. M. Kober. The Generalized Interpolation Material Point Method. *Computer Modeling in Engineering & Sciences*, 5(6):447–495, 2004.
[42] P. C. Wallstedt and J. E. Guilkey. Improved Velocity Projection for the Material Point Method. *Computer Modeling in Engineering and Science*, 19(3), 2007.
[43] S Leroch, SJ Eder, G Ganzenmüller, LJS Murillo, and MR Ripoll. Development and validation of meshless 3d material point method for simulating the micro-milling process. *Journal of Materials Processing Technology*, 262:449–458, 2018.
[44] L Gonzalez Acostaa, PJ Vardona, and MA Hicksa. An evaluation of mpm, gimp and cmpm in geotechnical problems considering large deformations. In *15th International Conference of the International Association for Computer Methods and Advances in Geomechanics*, 2017.
[45] Steve Plimpton. Fast parallel algorithms for short-range molecular dynamics. *Journal of computational physics*, 117(1):1–19, 1995.
[46] SJ Eder, Davide Bianchi, U Cihak-Bayr, and K Gkagkas. Methods for atomistic abrasion simulations of laterally periodic polycrystalline substrates with fractal surfaces. *Computer Physics Communications*, 212:100–112, 2017.
[47] M Varga, M Flasch, and E Badisch. Introduction of a novel tribometer especially designed for scratch, adhesion and hardness investigation up to 1000°c. *Proceedings of the Institution of Mechanical Engineers, Part J: Journal of Engineering Tribology*, 231(4):469–478, 2017.
[48] Frank Philip Bowden and JE Young. Friction of diamond, graphite, and carbon and the influence of surface films. *Proceedings of the Royal Society of London. Series A. Mathematical and Physical Sciences*, 208(1095):444–455, 1951.

Supplementary Material

Algorithm 1 Constant force algorithm using Proportional Integral (PI) Controller

while $t < t_{total}$ **do** ▷ Run simulation for a given time t_{total}
  for all $i \in \mathcal{S}_{indenter}$ **do** ▷ Sum up total force deviation in z-direction on indenter with particles i
    $dev \leftarrow \frac{f_z - F}{F}$
  end for

  $w \leftarrow \frac{\Delta t}{2T_i}$
  $old \leftarrow dev_{integral}$
  $new \leftarrow dev$
  $dev_{integral} \leftarrow w * old + (1 - w) * new$ ▷ Sum over all contributions within interval T_i in the PI controller

  $v_z \leftarrow Min(\frac{K_p}{\Delta t} * dev_{integral}, v_{max})$ ▷ Use displacement per time, v_z should not exceed v_{max}

  for all $i \in \mathcal{S}_{indenter}$ **do** ▷ Corrected velocities and positions in z-direction for the indenter particles
    $v_i \leftarrow v_z$
    $x_i \leftarrow x_i + \Delta t * v_z$
  end for
  $t \leftarrow t + \Delta t$ ▷ Increment elapsed simulation time
end while

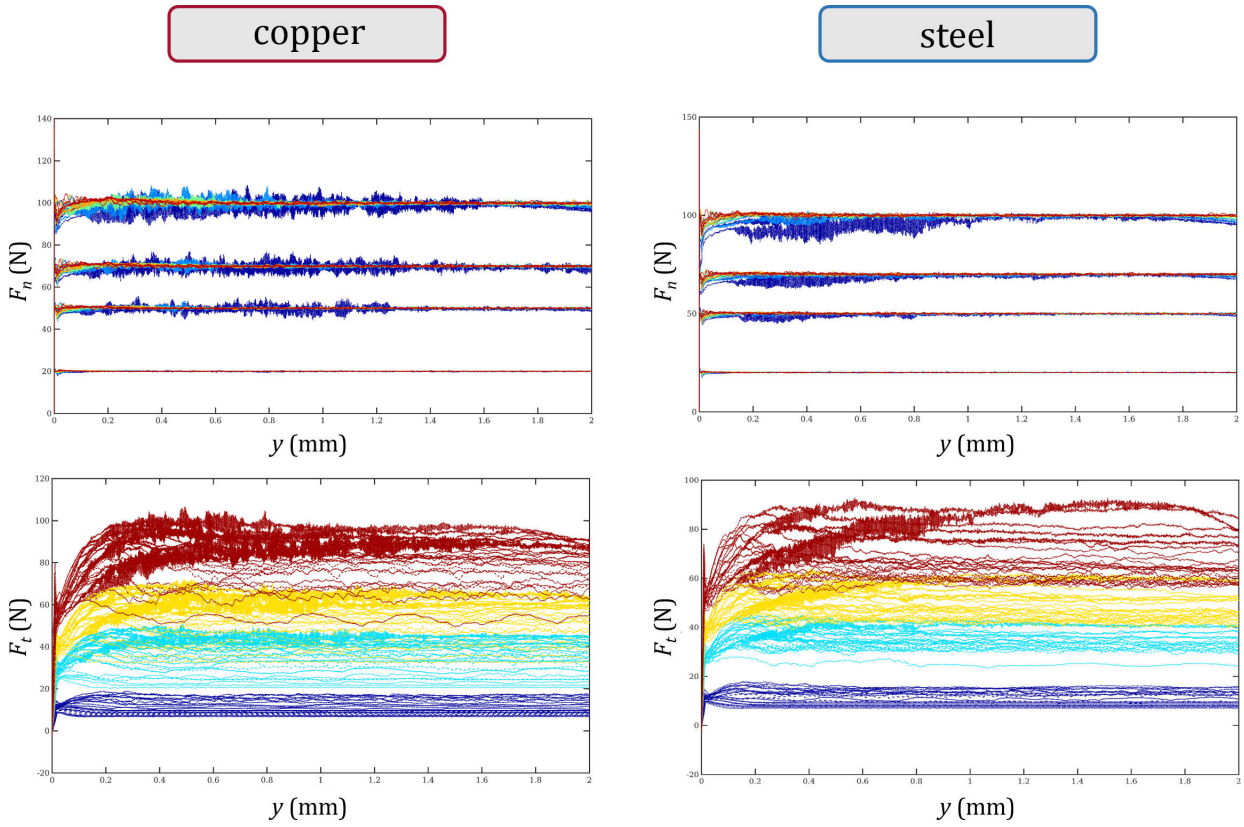

Figure S1: Simulated normal forces F_n and transverse forces F_t over the scratching distance y for copper and steel.

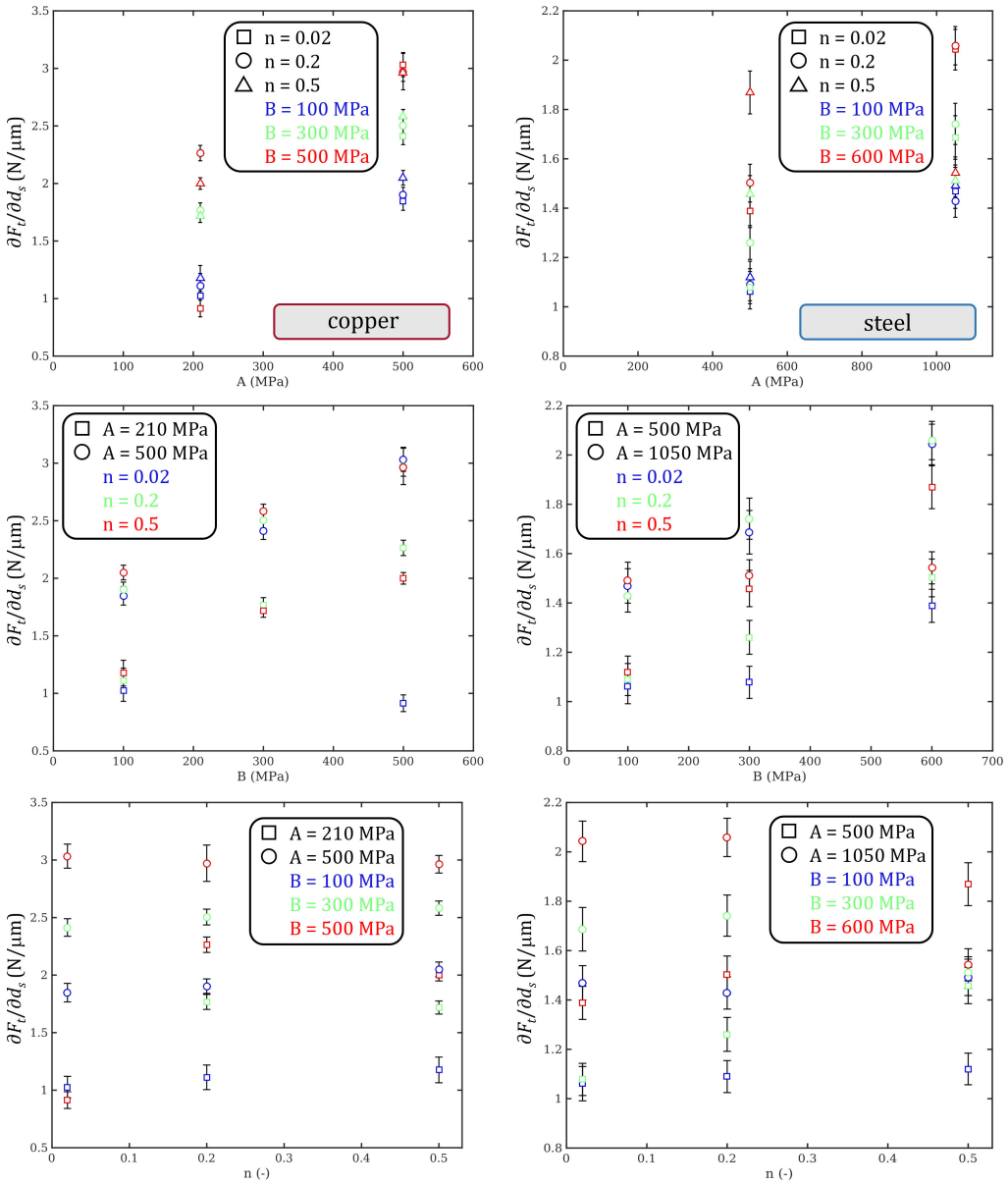

Figure S2: On the influence of n on the cutting force. Top: Colors stand for different values of B and symbols for different values of n

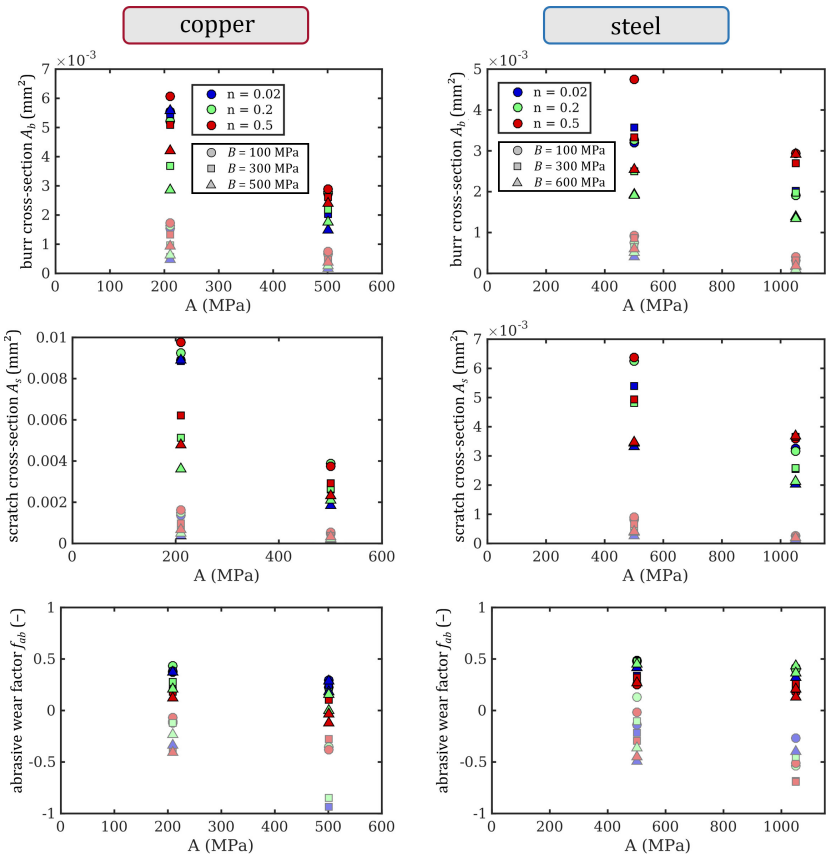

Figure S3: Cross-section areas of burr A_b and scratch A_s, as well as the abrasive wear factor f_{ab} as a function of A for various values of B and n. n is color-coded, and different values of B are represented as different symbols. Saturated symbols represent values recorded at 70 N, desaturated ones at 20 N.

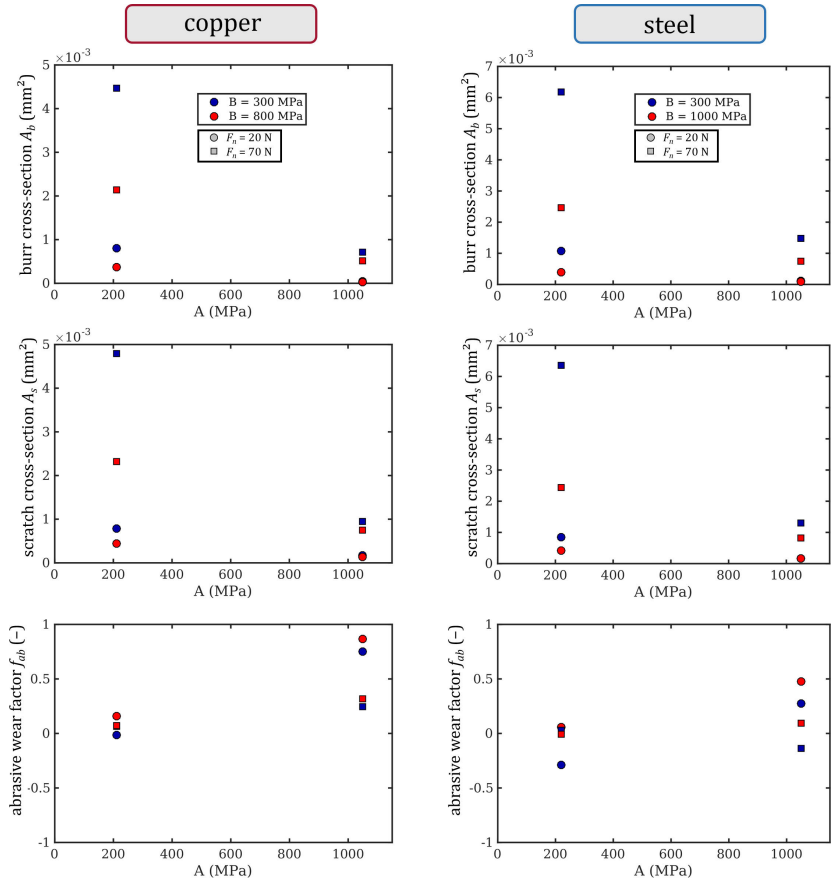

Figure S4: Cross-section areas of burr A_b and scratch A_s, as well as the abrasive wear factor f_{ab} with the Coulombic friction set to zero, as a function of A for various values of B. B is color-coded, and different normal forces F_n are represented as different symbols.

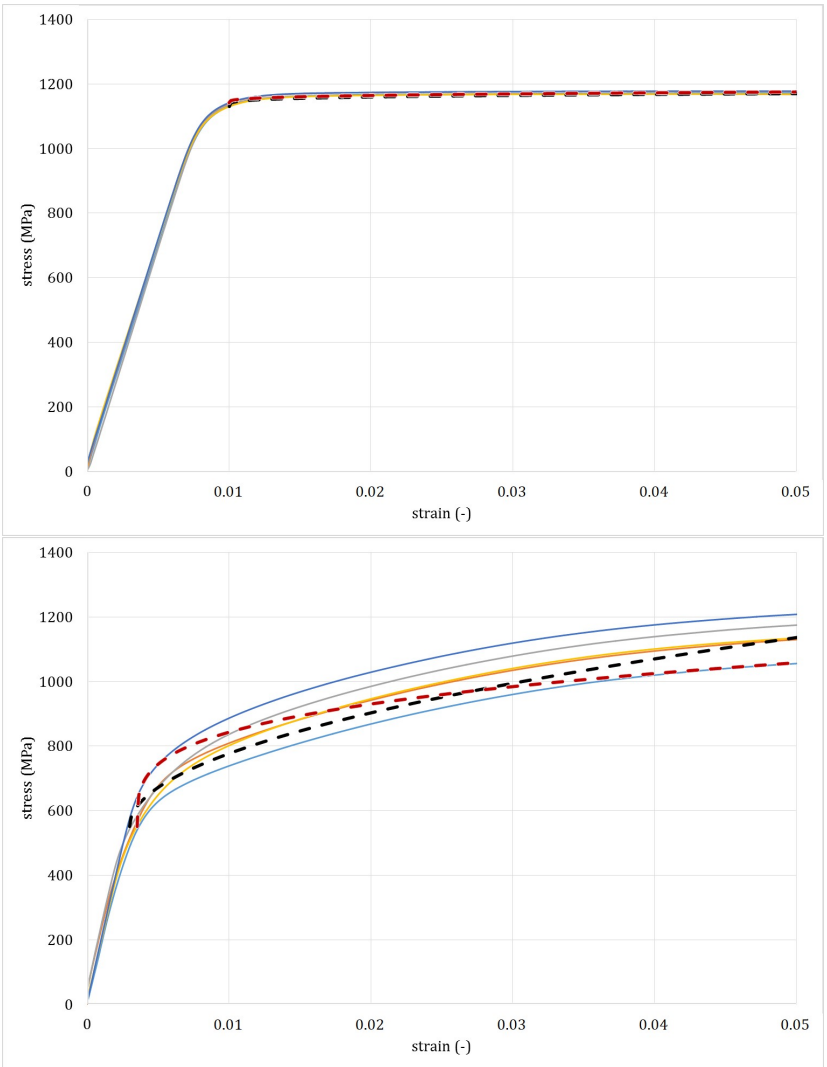

Figure S5: Stress-strain curves for CuNi alloy (top) and R260 steel (bottom) obtained from tensile tests. The dashed bold curves represent the fits to the data. The black curves were obtained by fitting all parameters including n, whereas for the red curves, n was kept constant at 0.28. Although this reduces the quality of fit for the steel sample, the results still lie within the variance of the experimental data.